Remote Sea Surface Temperature Variations during ENSO: Evidence for a Tropical Atmospheric Bridge

Stephen A. Klein

Program in Atmospheric and Oceanic Sciences, Princeton University, Princeton, New Jersey

Brian J. Soden and Ngar-Cheung Lau

Geophysical Fluid Dynamics Laboratory/NOAA, Princeton University, Princeton, New Jersey

ABSTRACT

In an El Niño event, positive SST anomalies usually appear in remote ocean basins such as the South China Sea, the Indian Ocean, and the tropical North Atlantic approximately 3 to 6 months after SST anomalies peak in the tropical Pacific. Ship data from 1952 to 1992 and satellite data from the 1980s both demonstrate that changes in atmospheric circulation accompanying El Niño induce changes in cloud cover and evaporation which, in turn, increase the net heat flux entering these remote oceans. It is postulated that this increased heat flux is responsible for the surface warming of these oceans. Specifically, over the eastern Indian Ocean and South China Sea, enhanced subsidence during El Niño reduces cloud cover and increases the solar radiation absorbed by the ocean, thereby leading to enhanced SSTs. In the tropical North Atlantic, a weakening of the trade winds during El Niño reduces surface evaporation and increases SSTs. These relationships fit the concept of an "atmospheric bridge" that connects SST anomalies in the central equatorial Pacific to those in remote tropical oceans.

1. Introduction

It is widely recognized that the air–sea coupled phenomenon known as the El Niño–Southern Oscillation (ENSO) has climatological impacts in regions far removed from the tropical Pacific. Perhaps the most well known of these remote impacts, generally designated as "teleconnections," are the changed atmospheric circulation over the northern Pacific and North America region and the associated sea surface temperature (SST) anomalies in the North Pacific (Wallace and Gutzler 1981; Deser and Blackmon 1995; Lau 1997). It has also been noted that SSTs in the Indian and Atlantic Oceans and near-surface air temperatures at land stations in the Tropics are also usually above normal when SSTs in the central and eastern Pacific are above normal (Chiu and Newell 1983; Pan and Oort 1983; Kiladis and Diaz 1989; Yulaeva and Wallace 1994; Tourre and White 1995; Lanzante 1996; Enfield and Mayer 1997). These changed surface temperatures are, in turn, associated with drought conditions in the northeast region of Brazil (Hastenrath et al. 1987) and in India (Rasmusson and Carpenter 1983; Wu and Hastenrath 1986).

A number of these authors have noted that SST anomalies in the Indian Ocean and the northern part of the tropical Atlantic generally lag those in the Pacific, thus suggesting that the warming in the oceans remote to the Pacific is related to forcing from the Pacific. Since the Indian and Atlantic Oceans are not directly connected to the Pacific Ocean, the explanation for these remote connections may lie in the "atmospheric bridge" mechanism considered by Lau and Nath (1996). This mechanism entails the forcing of the remote atmospheric circulation by the SST anomalies in the tropical Pacific, and the ensuing response of the remote oceans to such atmospheric changes. In this paper, it is our goal to document the processes that are responsible for these ENSO-induced SST anomalies in the remote tropical ocean basins. To do this, we will use over 40 yr of ship observations and 10–15 yr of satellite data to explore the nature of these remote tropical SST anomalies.

In the next section we define our ENSO index as well as the remote regions that have prominent teleconnections in SST. Section 3 provides an overview of the changes in tropical circulation associated with ENSO. Section 4 gives a region-by-region analysis of the remote changes in climate that are correlated with the ENSO index. Particular emphasis will be given to the changes in cloud cover and evaporation from the ocean that are correlated with the ENSO index. Section 5 describes a quantitative test of whether the observed anom-

Corresponding author address: Dr. Stephen A. Klein, Geophysical Fluid Dynamics Laboratory/NOAA, Princeton University, Forrestal Campus/U.S. Route 1, P.O. Box 308, Princeton, NJ 08542.
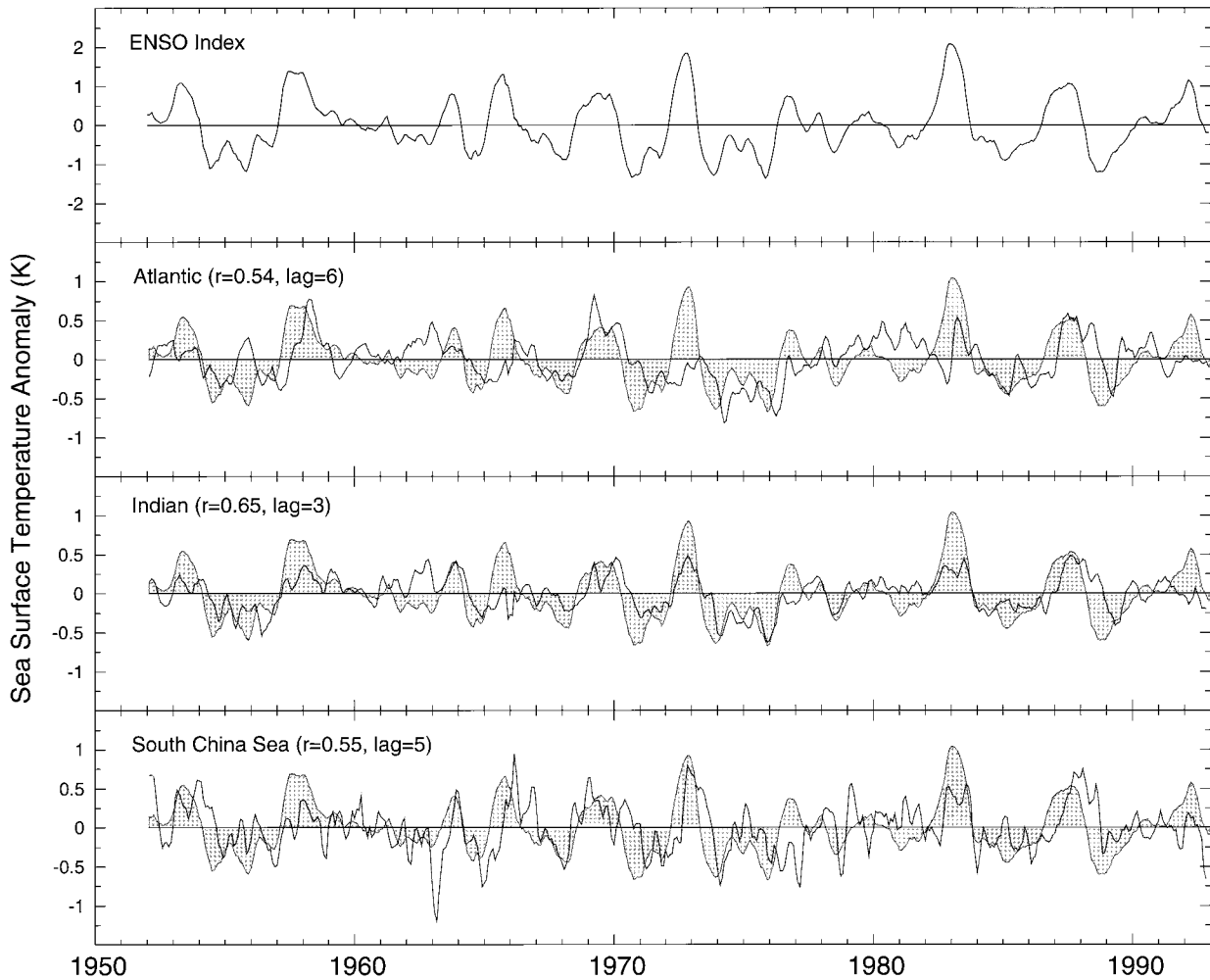E-mail: sak@gfdl.gov

FIG. 1. Time series of the ENSO index and SST anomalies in the tropical North Atlantic (5°–22.5°N, 17.5°–85°W), Indian Ocean (10°S–25°N, 45°–100°E), and South China Sea (2.5°–22.5°N, 100°–120°E). For each time series, the data have been smoothed using a 3-month running mean and the linear trend over the 41 yr has been removed. The shaded curve plotted with each SST time series is the ENSO index divided by 2. Above each SST time series is the value of the correlation coefficient between the ENSO index and the SST time series at the lag time corresponding to the maximum correlation coefficient. For example, the North Atlantic Ocean time series has a correlation coefficient of +0.54 with the ENSO index when the North Atlantic Ocean time series lags the ENSO index by 6 months.

alies in the ENSO-related net heat flux into the ocean are capable of explaining the lagged SST anomalies observed in these basins. Section 6 provides a brief summary of the main findings.

2. Correlation structure between remote surface temperatures and ENSO

Following several precedents (Deser and Wallace 1990; Fu et al. 1996), the time series of ship-observed SST anomalies was averaged for the region bounded by 5°N, 5°S, the South American coast, and 180° (see the appendix for the description of the ship data used). This time series was smoothed with a 5-month running mean and the linear trend over the 41-yr period (1952–92) was removed. This time series is defined as the ENSO index and is displayed in Fig. 1 (see top curve). An

alternative index, the time series of the first empirical orthogonal function (EOF) of tropical Pacific SST anomalies, was also considered. However, since the correlation coefficient between the EOF time series and the ENSO index is +0.90, results obtained using this alternative index are not substantially different from those presented here. Inspection of the ENSO index revealed seven events where the ENSO index exceed 1°C (1953, 1957–58, 1965, 1972–73, 1982–83, 1987, 1992) and six events where the ENSO index was less than −1°C (1954, 1955, 1970–1971, 1973, 1975, 1988). The warm events occur in all calendar months with a slight preference for June–September. However, the cold events occur primarily in the months of September–January, with no cold events occurring in March–May. The correlation coefficient between the ENSO index and the Southern Oscillation index (SOI; defined as the stan-

dardized sea level pressure difference between Darwin and Tahiti, and also smoothed by a 5-month running mean) is −0.67. The peak correlation occurs when the ENSO index is correlated with the simultaneous SOI.

Time series of SST anomalies averaged over the Indian Ocean (10°S–25°N, 45°–100°E), South China Sea (2.5°–22.5°N, 100°–120°E), and tropical North Atlantic (5°–22.5°N, 17.5°–85°W) are displayed in the lower part of Fig. 1. In general, peaks and troughs in the remote ocean SSTs lag those in the ENSO index by a few months. The magnitude of SST anomalies in the remote oceans is typically 0.2°–0.3°C. However, extreme peak anomalies may reach 0.5°C. Despite a good general relationship, not every El Niño or La Niña results in a peak or trough in the remote ocean time series (see Lanzante 1996). Furthermore, extremes in the remote ocean time series occur independently of ENSO. This suggests that although ENSO on average is related to SST anomalies in the remote oceans, ENSO is not the sole determining factor for the SST changes in these faraway sites. Inadequate sampling by ships may also contribute to the apparent variations in these time series.

To quantify the lag between the remote oceanic changes and the ENSO index, SST anomalies for each region were correlated with the ENSO index for lead–lag times ranging from minus 12 months to plus 12 months. The lead–lag time with the maximum correlation coefficient and the value of the correlation coefficient at that lead/lag time is displayed above each remote ocean time series in Fig. 1. Approximately 25%–35% of the interannual variability in SST in the remote regions is explained by variations in the ENSO index. Consistent with Lanzante (1996), the lag time is about 3 months for the Indian Ocean, and about 5 or 6 months for the tropical North Atlantic and South China Sea. The lag time for the Indian Ocean is also supported by the analysis of Charles et al. (1997) who showed that variations in δ^{18}O of coral from the Seychelles lagged pressure anomalies at Darwin by 3 months.

The simultaneous correlation coefficient between ENSO index and blended satellite–in situ observed SST anomalies (Reynolds and Marsico 1993) and the ship-observed SST anomalies is displayed in Figs. 2a,b, respectively. Correlations computed using empirically reconstructed ship SSTs (Smith et al. 1995) are very similar to those shown here. To focus on ENSO-scale variability, the time series of SST anomalies at each point was smoothed by a 3-month running mean and the linear trend over the length of the record was subtracted before calculating these correlation coefficients. Contemporaneous positive correlations exist between the ENSO index and SSTs in the Indian Ocean, the South China Sea, and the Atlantic Ocean. Note that several features of the correlation structure of the satellite SST do not appear in the correlation structure from the longer ship-observed SST record. These features include a strong negative correlation of equatorial Atlantic SST with the ENSO index and a very prominent correlation of SSTs

near Madagascar with the ENSO index. These differences may reflect the limited number of ENSO events covered by the satellite observations or the limited spatial sampling of the ship observations. Indeed, Lanzante (1996) demonstrated that the negative SST anomalies in the equatorial Atlantic are unique to the 1982–83 ENSO event. Also shown in Fig. 2b are the contemporaneous correlation coefficients between the ENSO index and the surface air temperature record at land stations (Jones et al. 1986). Positive correlations with the ENSO index occur over central and southern Africa, India, Indochina, and northwestern South America.

The remote correlations become even more prominent when the ship-observed SSTs and continental surface air temperatures lag the ENSO index by 4 months (Fig. 2c). The area covered by correlation coefficients exceeding 0.2 or 0.4 expands in the Indian Ocean while in the Caribbean and tropical North Atlantic the correlation coefficients increase from above 0.2 to above 0.4. Note that the magnitude of correlation coefficients in the Pacific equatorial cold tongue decreases. This indicates that SST anomalies in the remote ocean basins (Indian Ocean, South China Sea, and tropical North Atlantic) reach their peak intensity while the ENSO-anomalies in the Pacific are decaying.

3. Inferred changes in the tropical circulation during ENSO

It is well known that ENSO is associated with changes in both the atmospheric circulation and tropical SSTs. During the warm (El Niño) phase, convective activity in the western equatorial Pacific shifts eastward to the central and eastern Pacific. This shift in convection leads to an altered Walker circulation, with anomalous rising over the central and eastern equatorial Pacific and anomalous sinking over the western equatorial Pacific and Indonesian Archipelago (e.g., Julian and Chervin 1978; Oort and Yienger 1996). Coinciding with the shifting and weakening of the Walker cell is a strengthening of the local Hadley cell over the central Pacific. In this section we shall document the circulation changes throughout the tropical zone by analyzing the available satellite observations.

Figure 3a shows the simultaneous correlation coefficient between satellite-measured upper-tropospheric relative humidity (UTH) (Soden and Bretherton 1996) and the ENSO index for the period 1979–92. Variations in UTH are closely coupled to changes in the large-scale tropical circulation (Schmetz et al. 1995; Soden 1998), with positive (negative) UTH anomalies indicative of rising (sinking) motion. Inspection of Fig. 3a shows the UTH anomalies accompanying spatial displacements of the Walker cell, with positive correlations in an elongated band over the central and eastern Pacific and negative correlations over the Indonesian Archipelago. The elongated band of positive correlations along the equatorial Pacific is flanked by negative cor-

a 0 month lag: satellite/buoy

b 0 month lag: ship + land

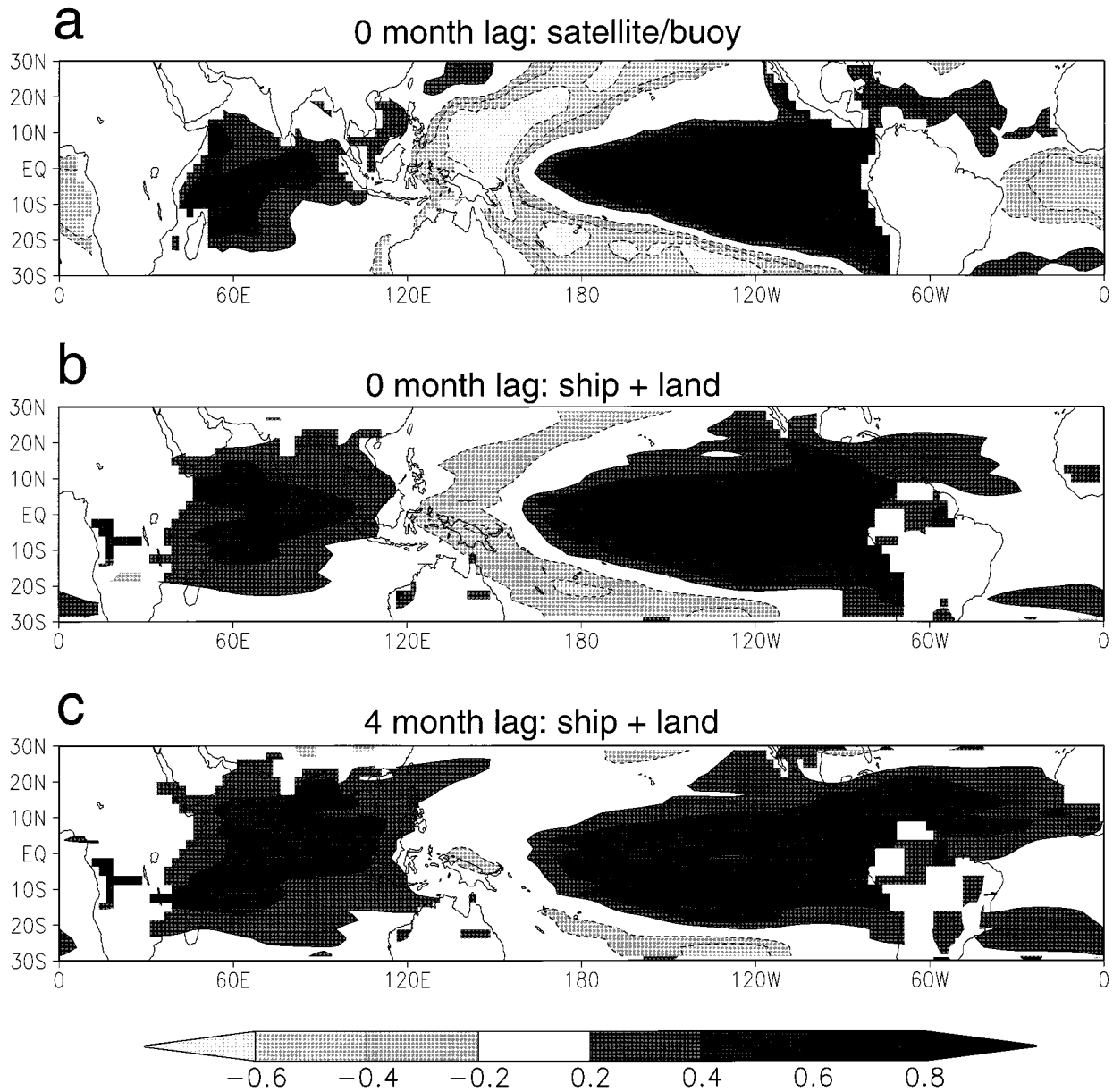

c 4 month lag: ship + land

FIG. 2. Maps of correlation coefficients between SST anomalies at each point and the ENSO index. (a) The correlation coefficients between satellite SST (Reynolds 1988) and the ENSO index for the period 1982–92. (b) The correlation coefficients between ship-observed SST and the ENSO index for the period 1952–92. Also included in this panel are the correlation coefficients between surface air temperature at land stations and the ENSO index for the period 1952–90. (c) The same as (b) but with SST and surface air temperatures lagging the ENSO index by 4 months. Prior to the calculation of correlation coefficients, the data at each grid point have been smoothed using a 3-month running mean.

relation to the north and south. This pattern reflects the enhanced local Hadley cell over the eastern Pacific during El Niño. Note, however, that the anomalies are not restricted to the Pacific basin. The tropical Atlantic shows that negative UTH anomalies occur along the equator with positive anomalies occurring to the north and south, thus suggesting a weakening of the local Hadley cell over the Atlantic during El Niño. A similar though less symmetric pattern is observed over the In-

dia–Indonesian region (60°–120°E). These structures suggest that the anomalous convection over the central Pacific strengthens the local Hadley cell, and also produces anomalous subsidence over Indonesia (via the altered Walker cell) and the equatorial Atlantic, thereby weakening the Hadley cell in these remote basins. Figure 4 illustrates a schematic of these inferred changes in the time-mean tropical circulation. This simplistic diagram highlights the circulation changes along the
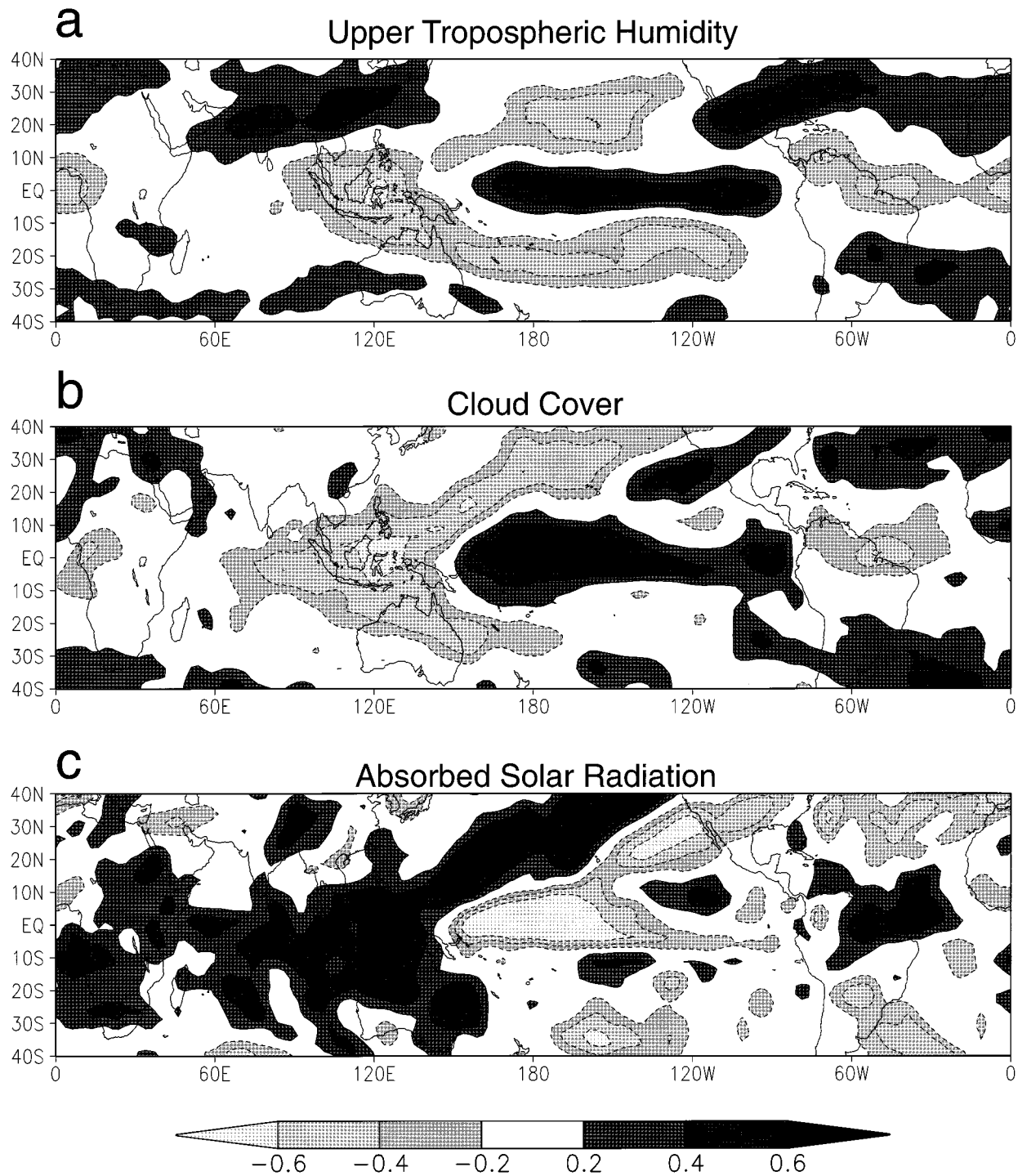
FIG. 3. Maps of correlation coefficients between the ENSO index and anomalies in several satellite-retrieved fields: (a) Upper-tropospheric humidity for the period 1979–92; (b) cloud cover from the International Satellite Cloud Climatology Project for the period 1983–90. (c) Top-of-atmosphere absorbed solar radiation from the Earth Radiation Budget Experiment for the period 1985–89. Prior to the calculation of correlation coefficients, the time series of satellite data have been smoothed using a 3-month running mean.
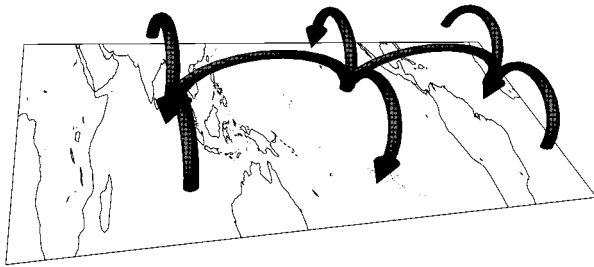
FIG. 4. Schematic diagram indicating some of the tropical changes in large-scale vertical motion that accompany El Niño events. Note that this diagram is not meant to exclude changes in midlatitude circulation that accompany El Niño, which may impact the Tropics.

local two-dimensional zonal or meridional planes. It should be noted that the anomalies in the three-dimensional flow field are generally not simply aligned along these two set of orthogonal planes.

Similar changes are also apparent in satellite observations of cloud cover and absorbed solar radiation. Figure 3b shows the correlation coefficients between the ENSO index and total cloud cover from the International Satellite Cloud Climatology Project (ISCCP; see Rossow and Schiffer 1991) for July 1983–June 1990. Figure 3c depicts the correlation between the ENSO index and Earth Radiation Budget Experiment (ERBE; see Harrison et al. 1989) observations of top-of-atmosphere absorbed solar radiation for February 1985–May 1989. Even though the time periods for the ISCCP and ERBE observations are shorter, the correlation patterns for clouds and absorbed solar radiation are remarkably consistent with those noted for UTH (Fig. 3a), indicating that cloud cover anomalies are strongly correlated with the inferred circulation anomalies, which, in turn, produce changes in absorbed solar radiation. The greater spatial variability in the correlation pattern for absorbed solar radiation may be attributed to the shorter time period of this dataset. It is not surprising to see that the increased convection over the central Pacific enhances cloud cover and reduces the absorbed solar radiation. However the circulation and cloud cover changes are not confined to the Pacific. Rather they extend over the adjacent equatorial Atlantic and Indian Oceans thereby acting as a "bridge" for connecting SST changes in the tropical Pacific to corresponding changes in these remote ocean basins. This hypothesis is further explored on a region-by-region basis in the next section using both satellite and surface observations.

4. Regional analysis

We begin our analysis with the South China Sea because it is geographically closest to the Pacific Ocean basin where the ENSO phenomena is most active. After discussion of the South China Sea we present the results for the tropical North Atlantic and the Indian Ocean. As seen below, the reason to separate the analysis of
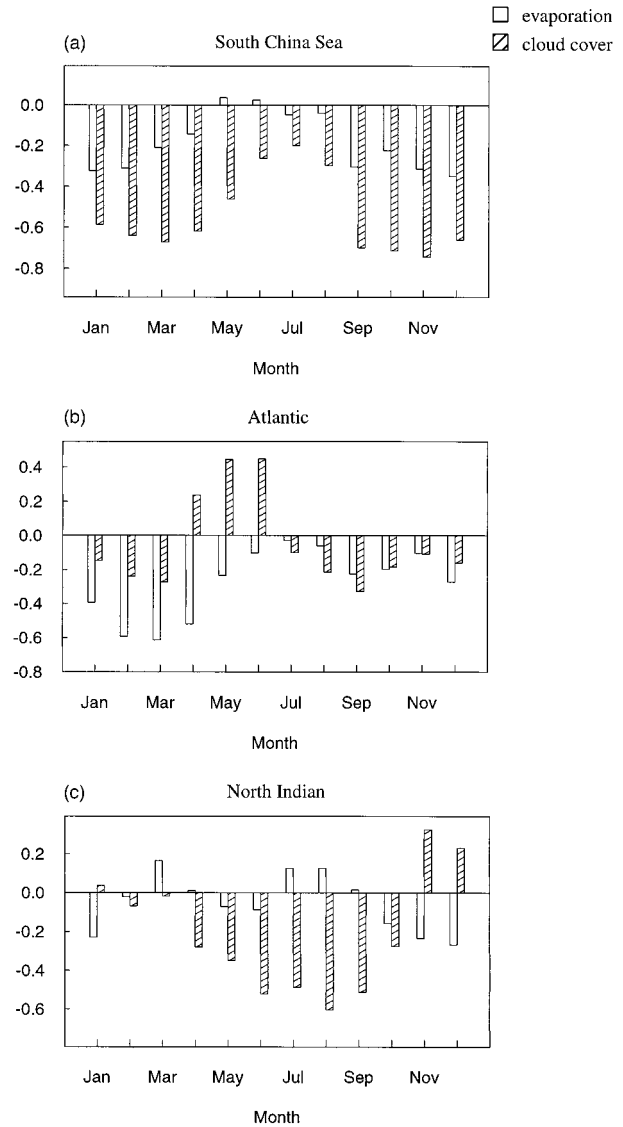

FIG. 5. Correlation coefficients for each calendar month between anomalies in evaporation (clear columns) and cloud cover (hatched columns) from ship observations (1952–92) and the ENSO index for the South China Sea, tropical north Atlantic, and Indian Ocean. The ocean areas encompassing each region are the same as in the caption to Fig. 1. Before calculation of the coefficients, the time series of evaporation and cloud cover anomalies were smoothed by a 3-month running mean and the linear trend over the 41 yr was removed.

the South China Sea from that of the Indian Ocean is the different nature of the teleconnections and their physical mechanisms.

a. South China Sea

One of the important aspects of ENSO-related teleconnections is that they exhibit a strong seasonal dependence. Figure 5a displays the correlation coefficients between evaporation or cloud cover anomalies from the ship observations (1952–92) in the South China Sea

(2.5°–22.5°N, 100°–120°E) with the ENSO index for each calendar month. (The method of computing evaporation from ship observations is explained in the appendix.) Cloud cover over most of this region typically decreases during El Niño as the South China Sea lies near the region of descent in the anomalous Walker cell (Fig. 3). The best relationship exists for the calendar months of September–April. During El Niño, evaporation in the South China Sea also decreases during these same months, however, the relationship is not as strong as for cloud cover. Visual inspection of time series from the satellite data (Fig. 6) also reveals a distinct reduction in cloud cover during El Niño. During the first three months of 1987, the clouds cover nearly 12% less area than normal while shortwave radiation absorbed at the top of atmosphere is over 12 W m⁻² above normal. Opposite but weaker anomalies prevailed during La Niña conditions of 1984–86 and 1988–89. The cloud cover and solar radiation changes are coincident with the ENSO index, while the SST change lags the index by ∼6 months. This suggests that the cloud cover changes respond immediately to the warming of the tropical Pacific (via the atmospheric "bridge"), whereas the local ocean surface warming is delayed due to its thermal inertia (see section 5).

To study more closely the changes in circulation, we present in Figs. 7a,b the typical anomalies in the ship-observed surface wind field, latent heat flux, and cloud cover during boreal winter that accompany an El Niño. These anomalies were calculated by regressing the monthly mean anomalies from October through March on the ENSO index, and scaling the resulting slopes by the standard deviation of the ENSO index. Thus the anomalies shown in Fig. 7 represent the typical anomalies present when the ENSO index is one standard deviation above normal. During El Niño, there are anomalous southerlies or southwesterlies in the South China Sea. This anomalous circulation opposes the mean wintertime northeasterly flow that advects cold and dry air off the Asian continent. With anomalous southerlies or southwesterlies, one could expect both a reduction in the mean surface wind speed and the occurrence of cold-air outbreaks. Accordingly, the latent (Fig. 7a) and sensible (not shown) heat flux in the northern portion of the South China Sea as well as the region northeast of the Philippines are significantly reduced.

There is a reduction of cloud cover of near 3% during winter when the ENSO index is high (Fig. 7b). The location of the peak reduction in cloud cover based on ship observations is almost the same as that of the peak negative correlation between satellite cloud cover and the ENSO index (Fig. 3b), thus installing confidence in both the satellite and surface observations of clouds. It is interesting to note that reduced cloud cover also occurs in the eastern portions of the Indian Ocean. With a combination of increased solar heating and reduced evaporative cooling over the South China Sea, one expects that the net heat flux into the ocean is increased in an El Niño.

To infer typical anomalies in the net heat flux entering the oceans, we estimate changes in the sum of solar radiation entering the ocean and the sensible and latent heat flux leaving the ocean. In the absence of an accurate method for computing the net longwave cooling using ship data, we neglect this component in the following discussion. Fortunately the lower tropical troposphere has a thick opacity due to high amounts of water vapor in that layer, consequently the net longwave cooling of the surface is relatively insensitive to variations in cloud cover or UTH (Inamdar and Ramanathan 1994). To estimate the change in surface solar radiation we use the parameterization of Reed (1977)

$$SW = SW*(1 - 0.62C), \quad (1)$$

where SW is net surface solar radiation (W m⁻²), SW* the net solar radiation incident at the surface under clear skies, and C is the fractional cloud cover. Assuming a typical tropical value for SW* of 305 W m⁻² and ignoring its small seasonal variation, (1) simplifies to

$$SW' = -2C', \quad (2)$$

where SW′ is the anomaly in net surface solar radiation in units of W m⁻² and C' is the anomaly in cloud cover in percent. The procedure for computing the sensible and latent heat flux is given in the appendix. The sum of typical anomalies of net solar radiation at the surface, evaporation, and sensible heat are shown in Fig. 7c. This pattern indicates an increase of 8–10 W m⁻² in the South China Sea when the ENSO index is high. In the southern portion of the South China Sea, most of this increase is due to the reduced cloud cover, while in the northern portion reduced latent heat flux makes a contribution comparable to the reduced cloud cover. It is interesting to note that the region to the northeast of the Philippines, which has a positive 12 W m⁻² anomaly in the net heat flux, does not show a strong lag correlation of SST to the ENSO index (Fig. 2). In this portion of the Pacific, it is possible that oceanic wave dynamics associated with ENSO in that ocean act to damp effects of this heat flux anomaly. It is also noteworthy that a reduction in both latent heat flux and cloud cover in the southeast Indian Ocean leads to an increase of 8 W m⁻² in the net heat flux.

b. Atlantic sector

In the tropical North Atlantic (5°–22.5°N, 17.5°–85°W), changes in evaporation appear to have a stronger effect than changes in cloud cover. The middle of Fig. 5 indicates relatively strong negative correlations between evaporation and the ENSO index during the first four calendar months. The figure also indicates that the correlation between cloud cover and the ENSO index is negative and rather weak in most months. A notable exception is the April–June period, during which the
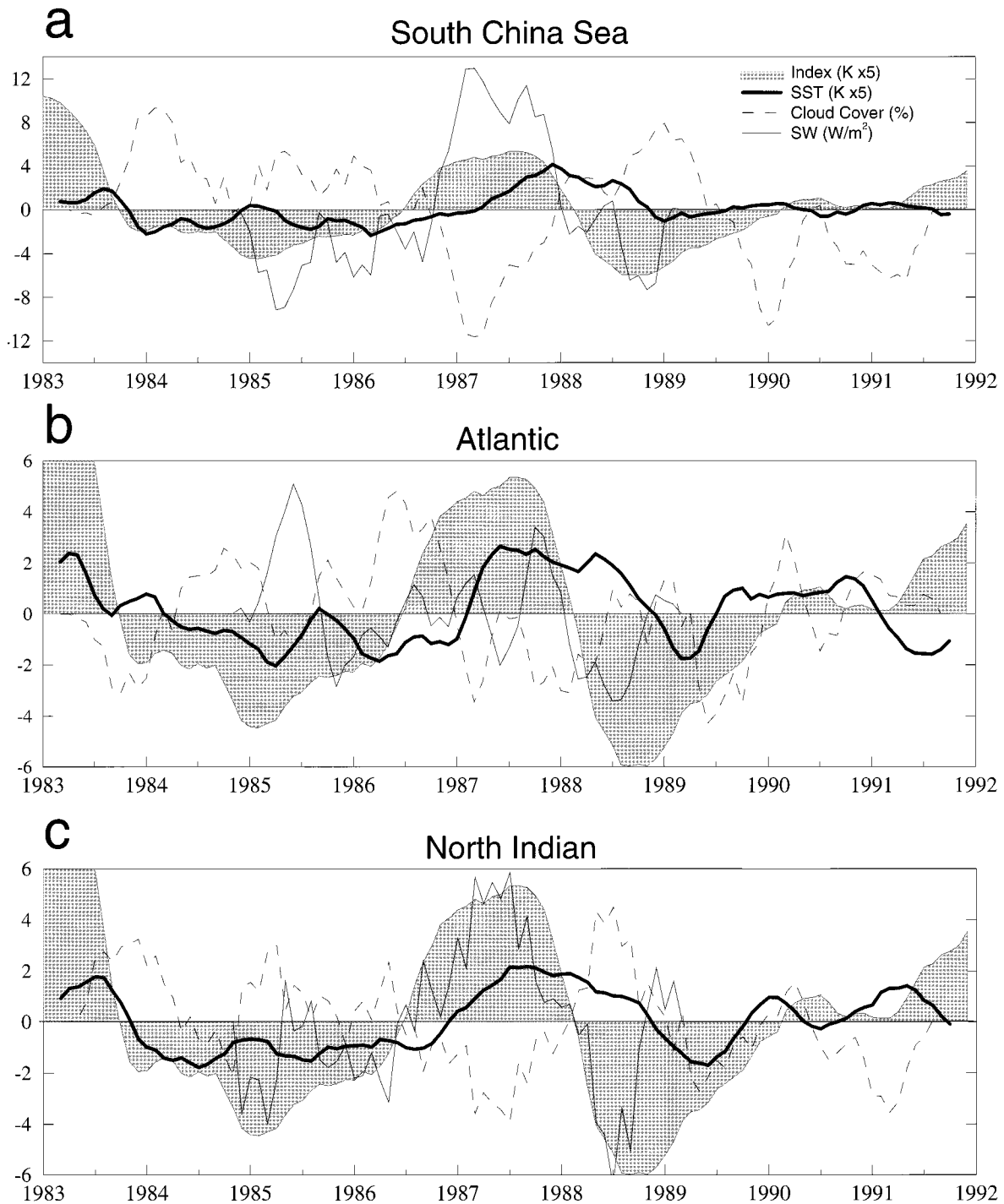
FIG. 6. Time series of the ENSO index and anomalies in satellite-observed SST, cloud cover, and absorbed shortwave radiation for the South China Sea, tropical North Atlantic, and Indian Ocean. The time series of SST, cloud cover, and absorbed shortwave radiation have been smoothed by a 5-month running mean.

ENSO index exhibits high, positive correlations with cloud cover. In addition, changes in cloud cover associated with ENSO tend to be modest and are largely restricted to the southern portion of this sector (Fig. 3c). Consequently, when averaged over the entire tropical

North Atlantic domain, the satellite-observed cloud cover exhibits relatively little correlation with the ENSO index compared to other basins (Fig. 6b). Figure 8 displays the typical anomalies in the ship-observed surface wind field, latent heat flux, and cloud cover during the

(a)   Evaporation and Surface Winds

(b)   Cloud Cover

(c)   Net Heat Flux

(a)   Evaporation and Surface Winds

(b)   Cloud Cover
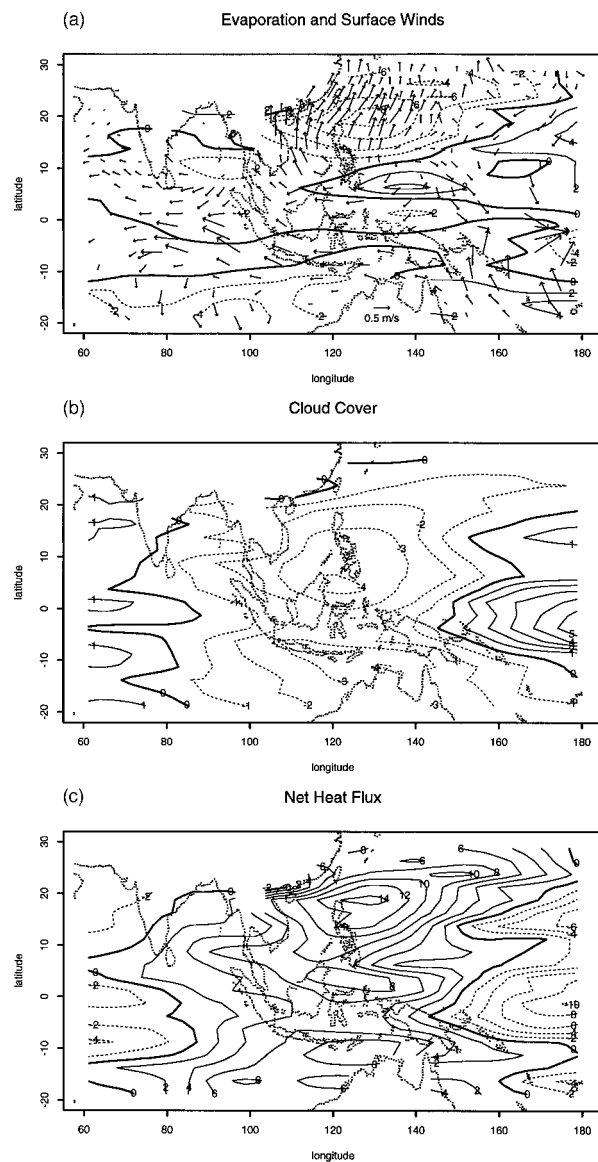

(c)   Net Heat Flux

FIG. 7. Typical October–March anomalies that accompany above normal conditions of the ENSO index. (a) The anomalies in vector mean surface wind (see reference vector plotted over northern Australia) and latent heat flux, in W m^{-2}, deduced by the bulk formulas. (b) The anomalies in ship-observed cloud cover in percent. (c) The anomalies in inferred net heat flux into the ocean in W m^{-2}. The anomalies are computed by regressing the ship observations for the months of October–March in the period 1952–92 upon the ENSO index and scaling the resulting slopes by the standard deviation of the ENSO index to yield quantities with physical units. Before calculation of the anomalies, the time series of surface winds, latent heat flux, and cloud cover anomalies at each point were smoothed by use of a 3-month running mean and the linear trend over the 41 yr was removed.
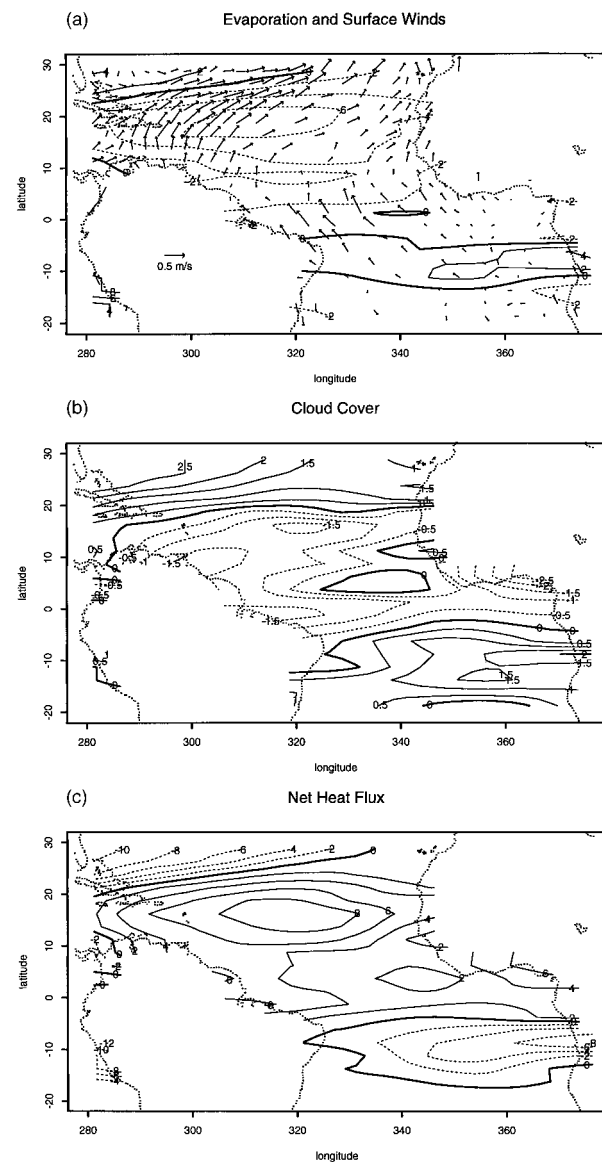
FIG. 8. As in Fig. 7 but for anomalies in the tropical Atlantic for the calendar months of January, February, March, and April in the years 1952–92. A reference wind vector is plotted over South America.

calendar months of January, February, and March that accompany an El Niño. For surface wind, the most prominent ENSO signal in the Atlantic sector is the anomalous southwesterlies over the Caribbean Sea and the central North Atlantic near 20°N. At latitudes south

of 20°N, these southwesterlies oppose the mean trade wind easterlies, leading to a reduction in wind speed (Enfield and Mayer 1997). Correspondingly, there is a reduction of 6 W m^{-2} in latent heat flux in the north-central tropical Atlantic. Although the correlation coefficient is weak, ship observations indicate a modest reduction of cloud cover in the tropical North Atlantic flanked by modest increases in cloud cover to the north and south. North of the equator, these cloud cover changes are consistent with the satellite data in Fig. 3. The disagreement south of the equator may reflect poor spatial sampling by ships or a differing response to ENSO in this region during the 1980s as compared to

the longer ship-based record (recall from Fig. 2 the difference in satellite and ship SSTs in this region). The typical anomalies in the net heat flux into the ocean (lower panel of Fig. 8) indicate an increase of over 8 W m^{-2} in the tropical Atlantic in the approximately the same location as that of the positive correlation of SST with the ENSO index (lower panel of Fig. 2).

What is the cause of the reduced trade winds in the North Atlantic? One possible mechanism is the anomalous low pressure center that is located over the southeast United States and is associated with changes in the Pacific–North American (PNA) pattern (Wallace and Gutzler 1981). Indeed, the calendar months with the strongest correlation between the latent heat flux (and by inference, the trade winds) over the North Atlantic and the ENSO index are January–April (Fig. 5), the same months when the PNA pattern has the strongest connection to ENSO. Thus the seasonality of the latent heat flux anomalies suggests that the PNA is involved. Further evidence for the role of the PNA is presented by Nobre and Shukla (1996). Weakened trade winds in the North Atlantic would also be associated with a reduction in the strength of the Hadley cell over the Atlantic sector as suggested by the pattern of UTH anomalies (Fig. 3).

c. Indian Ocean sector

One of the most well-known relationships about ENSO is that the Indian summer monsoon is typically weaker than normal in advance of the appearance of positive SST anomalies in the central equatorial Pacific (Angell 1981; Rasmusson and Carpenter 1983; Meehl 1987; Trenberth and Shea 1987; Webster and Yang 1992; Lau and Yang 1996a). The bottom of Fig. 5 indicates that the ship-observed cloud cover over the northern Indian Ocean (10°S–25°N, 45°–100°E) from 1952 to 1992 is negatively correlated with the ENSO index during the calendar months of April–September. Consistent with the previous studies, our ship-observed summertime cloud cover anomalies exhibit an even stronger relationship with the ENSO index when the ENSO index is lagged by 3 months relative to the cloud cover anomalies (not shown). The bottom of Fig. 6c shows the record of satellite-observed cloud cover and absorbed solar radiation over the northern Indian Ocean. Near April 1987, cloud cover over the Indian Ocean decreased by 4% while the amount of solar radiation absorbed increased by nearly 6 W m^{-2}. This occurred in advance of both the ENSO index and the peak SST anomaly in the Indian Ocean. The opposite scenario occurred near April of 1988.

The changes in April–September of surface winds, latent heat flux, cloud cover, and net heat flux associated with the ENSO index are displayed in the regression charts in Fig. 9. The computational procedure for constructing these charts is similar to that for Figs. 7 and 8, except that the ENSO index is lagged relative to all
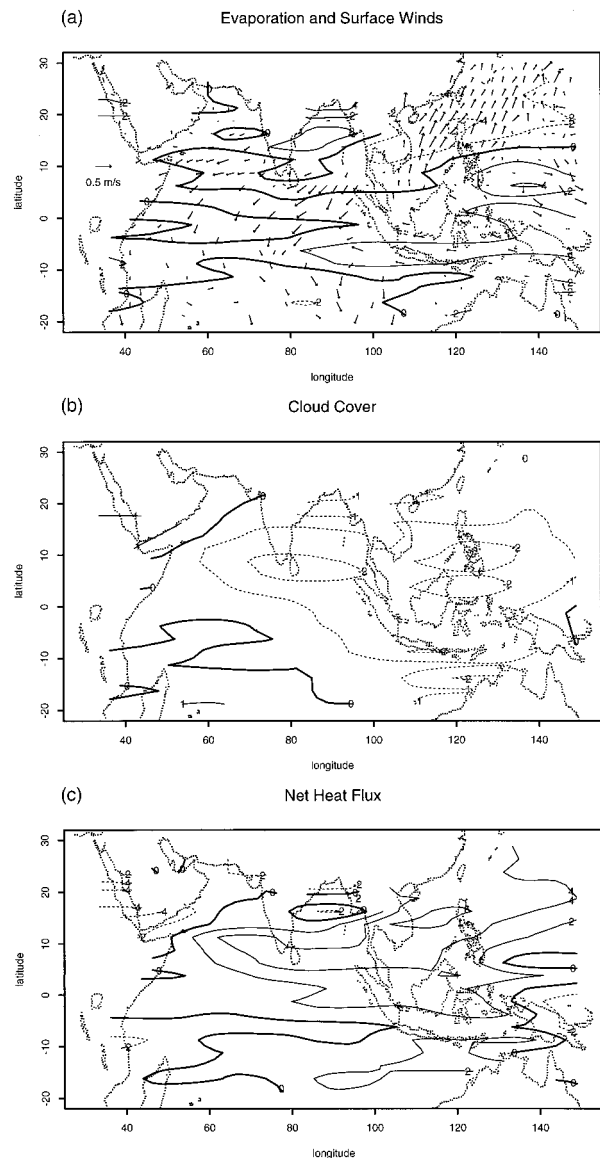

FIG. 9. As in Fig. 7 but for anomalies in the Indian Ocean for the calendar months of April, May, June, July, August, and September in the years 1952–92. The regression was performed with the ENSO index lagging the anomalies by 3 months. A reference wind vector is plotted over eastern Africa.

other fields by 3 months, in view of the phase relationship evident in Fig. 6c. In the Indian Ocean a belt of anomalous easterlies appears near 10°N and anomalous northerlies occur closer to the equator. The general wind pattern is contrary to the climatological summer monsoon wind pattern and indicates a weakening of the normal monsoon flow. Consistent with this weakened monsoon flow is reduced cloud cover over the southern tip of India and the Bay of Bengal, the regions with typically the most summer rainfall according to Microwave Sounding Unit data (Lau and Yang 1996b). Given the weak changes in both latent heat flux and cloud

cover, the standard anomalies in net heat flux are also quite weak with an increase in net heat flux of only 4 W m^{-2} in a band near 10°N, where the reduction in cloud cover is largest. It is interesting to note that the region of positive heat flux anomalies does not cover the whole of the Indian Ocean that has prominent correlations of SSTs to the ENSO index (cf. Figs. 7c and 9c with Fig. 2). Particularly absent are any positive heat flux anomalies in the southwestern Indian Ocean near Madagascar. It is possible that the SST anomalies in that region are the response to ocean dynamics instead of surface heat fluxes. Alternately, the discrepancy between the anomaly patterns in SST and surface heat flux may also be attributed to the limited number of ship observations in that portion of the Indian ocean, thus reducing the accuracy of the heat flux estimates.

5. Do the observed SST anomalies result from the surface heat flux anomalies?

In nearly all of the regions that show *lagged* correlations of SST relative to the ENSO index, we have demonstrated that there are changes in cloud cover or evaporation occurring either simultaneously with, or in advance of (as is the case with the Indian Ocean), the ENSO index. These changes drive SST anomalies of the same sign as those observed. Such variations in cloud cover or evaporation are stronger in certain calendar months, thus leading to the seasonal dependence of the resulting SST anomalies.

Suppose that the SST anomalies in the remote ocean basins are the response to changes in the local cloud cover and evaporation, and that they satisfy the following equation:

$$\frac{\partial}{\partial t}\text{SST}' = (F'/\rho cH) - (\text{SST}'/\lambda), \qquad (3)$$

where SST$'$ is the SST anomaly, F' is the anomaly in the surface net heat flux that is related to ENSO, ρ is the density of seawater, c is the specific heat of seawater, H is the oceanic mixed layer depth, and λ is the damping timescale for SST anomalies. The physical process represented by the damping term could be advection of the anomalous vertical temperature gradient by the mean entrainment of water from beneath the thermocline (Frankignoul 1985) or any other process unrelated to ENSO that restores the SST to its climatological value. (Note that in our equation the sensible and latent heat flux are part of the forcing, instead of part of the damping as is commonly assumed in mixed layer budget analyses.) Consider the case where the ENSO-induced anomaly in net heat flux depends on calendar month according to

$$F' = 10\,\text{W m}^{-2}$$
$$\times [\text{ENSO}(t)$$
$$\times \delta(\text{month} \in \{\text{January, February, March, April}\})$$
$$+ \varepsilon(t)], \qquad (4)$$

where ENSO(t) is the normalized time series of the ENSO index, $\varepsilon(t)$ is a time series of normally distributed random numbers with zero mean and unit variance, and the Kronecker delta, δ, is 1 if the calendar month falls between January and April and zero otherwise. Equation (4) states that the heat flux anomaly is determined by noise except during the calendar months of January–April, when the heat flux anomaly depends also on the state of ENSO. This specification for heat flux anomaly could reasonably portray the case for the tropical north Atlantic Ocean where the evaporation is strongly linked to the state of ENSO only in the calendar months of January–April (middle of Fig. 5). With heat flux anomalies given by (4), we numerically integrated (3) from January 1952 starting with zero SST anomaly to December 1992 using the observed time series of the ENSO index (Fig. 1), a mixed layer depth of 50 m (Levitus 1982), and a damping timescale of 12 months. The results presented below were performed with a single sequence of random numbers, $\varepsilon(t)$; however, runs with different sequences yield qualitatively similar results.

To examine the seasonal dependence of the SST anomalies simulated by (3), we correlated the simulated time series of net heat flux anomalies from (4) and SST anomalies from (3) with the ENSO index. This correlation was performed for each calendar month separately. For each calendar month we also correlated the anomalies in net heat flux or SST with the values of the ENSO index for various lead–lag times. For each correlation we computed the typical anomaly (as in Figs. 7–9) by calculating the regression slope of the heat flux or SST anomaly on the ENSO index and then scaling the slope by the standard deviation of the ENSO index. We contoured these typical anomalies in heat flux and SST in Fig. 10 as a function of the calendar month of the heat flux or SST anomaly and the lead–lag time between the anomaly and the index (positive lag indicates that the heat flux or SST anomaly lags the ENSO index). Figure 10a indicates that the March heat flux anomalies simulated from (4) are best correlated with the ENSO index (with a typical magnitude of 8 W m^{-2}) and that these March heat flux anomalies are best related to the value of the ENSO index one month prior. This is, of course, approximately the relationship we specified through (4). Figure 10c indicates that the June SST anomalies simulated from (3) when using (4) are best correlated with the ENSO index (with a typical magnitude of 0.25°C) and that these June SST anomalies are best related to the values of the ENSO index 3 months prior (i.e., the preceding March). The time delay of 3 months is a consequence of the thermal inertia of the ocean mixed layer. The simulated SST anomalies are not too sensitive to the damping timescale as integrations using a doubled or halved timescale shifted the calendar month or lag time with the maximum SST amplitude by only 1 month. Runs with different $\varepsilon(t)$ can also shift the pattern by 1 month in lag time or calendar
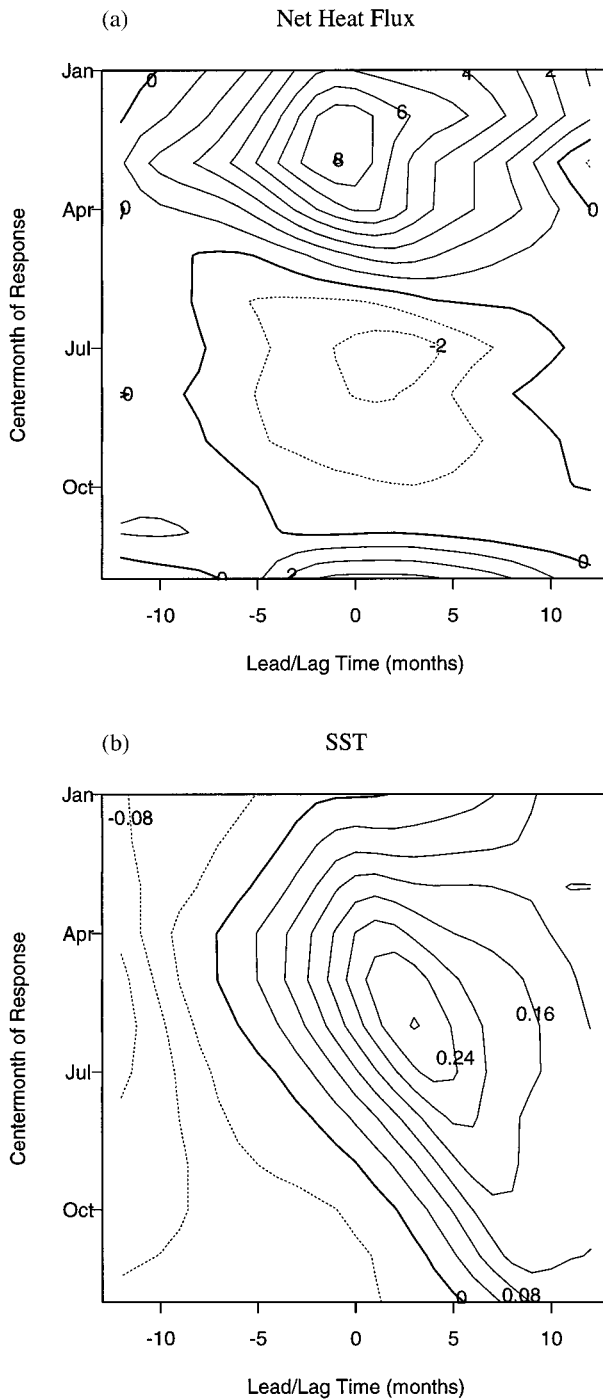
(a)   Net Heat Flux

(b)   SST

FIG. 10. Typical anomalies in a time series (a) of heat flux (W m^{-2}) and (b) SST anomalies (°C) that occur when the ENSO index is above normal, as simulated using (3) and (4). The anomalies are plotted as a function of the calendar month in which they occur and the lead–lag time relative to the ENSO index. Positive lag indicates that the heat flux or SST anomalies lag the ENSO index.

month. The above results confirm that *if the teleconnection of ENSO to the remote ocean depends on calendar month then the resulting SST anomalies should also depend on calendar month.* We proceed to further examine the SST response to seasonally varying forcing with real data.

We took the 41-yr record of net heat flux anomalies and SST anomalies for a portion of the tropical North Atlantic region (5°–22.5°N, 17.5°–60°W) and computed the typical anomalies that accompany variations in the ENSO index as was done in Fig. 10. The result (Fig. 11) is similar to Fig. 10 in both pattern and amplitude. The figure indicates that anomalies in the net heat flux are best correlated with the ENSO index when the anomalies are from the calendar months of January–April and when these anomalies are correlated with the simultaneous value of the ENSO index. The figure also indicates that SST anomalies in this region are best correlated with the ENSO index when the SST anomalies are from the calendar months of April and May and when these SST anomalies are correlated with the values of the ENSO index from four months prior (i.e., the proceeding January or February). This seasonality of latent heat flux and SST anomalies in the tropical North Atlantic is consistent with the data presented by Nobre and Shukla (1996) and Enfield and Mayer (1997). The similarities between the correlation structure based on simulated data (Fig. 10) and observations (Fig. 11) suggest that the observed SST anomalies are a direct response to the observed variations in the net heat flux. We note that this test demonstrates only that the observed SST and heat flux time series are both related to the ENSO index in a manner that is consistent with (3); this test does not address how much variance in remote SST time series is due to local variations in the net heat flux.

Providing that the damping term is small, (3) indicates that there should be a good correlation between the time series of SST tendency and the time series of the heat flux anomalies. We formed a tendency time series by subtracting the observed SST anomaly of the previous month from that of the subsequent month. This tendency time series for the tropical north Atlantic was also correlated with the ENSO index and its correlation structure is shown in Fig. 12. The strong similarity between Fig. 12 and Fig. 11a offers additional evidence that the ENSO-related SST anomalies are responding to variations in the net heat flux driven by ENSO. As a quantitative measure of the goodness of fit, we correlated the data values displayed in Fig. 12 with those in Fig. 11a. We note that this test does not use an assumed damping timescale or mixed layer depth. The correlation coefficient is fairly high (Table 1, row 2), indicating that the ENSO index is best correlated with both the SST tendency and the heat flux at zero time lag. One can infer a mixed layer depth from the magnitudes of the heat flux anomalies and the SST tendencies plotted in Figs. 11 and 12. For this region the inferred mixed layer
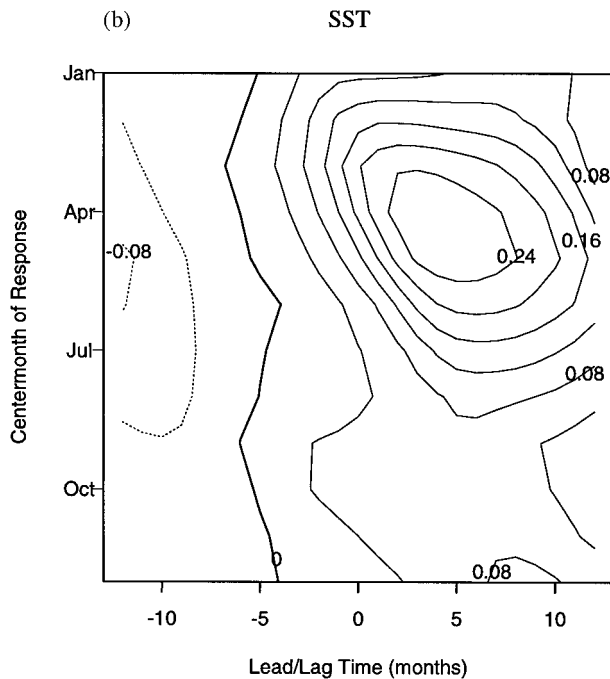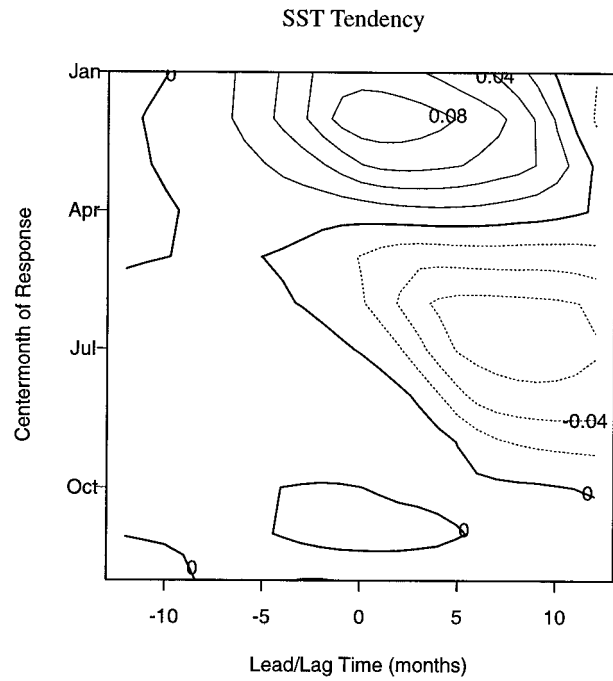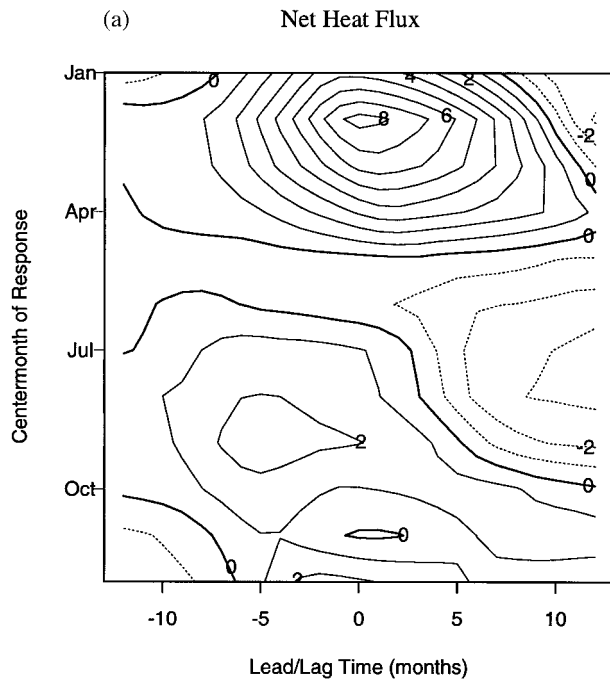
(a) Net Heat Flux

(b) SST

FIG. 11. As in Fig. 10 except that the time series are taken from ship observations of the inferred heat flux and SST anomalies from a portion of the tropical North Atlantic (5°–22.5°N, 17.5°–60°W).

depth is about 50 m, which is in fair agreement with that of the Levitus (1982) climatology.

We calculated identical figures to those in Figs. 11 and 12 for the other regions in the Tropics. We subdivided the Atlantic and Indian Oceans to provide addi-

SST Tendency

FIG. 12. As in Fig. 11 except that the time series is the SST tendency (°C month⁻¹) from a portion of the tropical North Atlantic (5°–22.5°N, 17.5°–60°W).

tional independent tests. Table 1 displays the correlation coefficients between panels of SST tendency and heat flux anomalies, the inferred mixed layer depths from the regression, and values of the mixed layer depth from the Levitus climatology. For the Atlantic Ocean, South China Sea, and most of the Indian Ocean, the high correlations (Table 1) suggest that heat flux anomalies cause the ENSO SST anomalies. The values of mixed layer depth are comparable to the corresponding observed values with the exception of the eastern portion of the

TABLE 1. Correlation coefficients between the correlation structures of SST tendency and heat flux anomalies. Also shown are the mixed layer (ML) depths (in meters) implied from this regression and observations of ML depth from the Levitus (1982) climatology for March (September) (Shaw et al. 1996*).

Region	Correlation	ML depth	Observed ML depth
Caribbean (9°–22.5°N, 60°–85°W)	0.83	55	75 (40)
north tropical Atlantic (5°–22.5°N, 17.5°–60°W)	0.89	45	60 (30)
northeast Indian Ocean (0°–25°N, 77.5°–100°E)	0.72	75	40 (35)
northwest Indian Ocean (0°–25°N, 45°–77.5°E)	0.77	55	30 (60)
southeast Indian Ocean (0°–20°S, 77.5°–100°E)	0.68	65	25 (50)
southwest Indian Ocean (0°–20°S, 45°77.5°E)	0.59	65	35 (60)
South China Sea (2.5°–22.5°N, 100°–120°E)	0.71	80	50–100*

Indian Ocean. For this region, it is possible that our heat flux anomalies are overestimated (perhaps because of errors in the Reed solar radiation parameterization). For the southwestern part of the Indian Ocean, the correlation structure of the heat flux anomalies does not exhibit a strong resemblance to the correlation structure of the SST tendency, suggesting that the SST anomalies there may result from other processes. These are the same regions that were found not to have a strong signal in cloud cover or evaporation anomalies (section 4c). Apart from the southwestern Indian Ocean, we conclude that the ENSO-related SST anomalies in the remote oceans result from heat flux anomalies associated with changes in evaporation and cloud cover during ENSO.

6. Final remarks

It is a remarkable fact that in warm (cold) phases of ENSO events, SSTs in the tropical North Atlantic, South China Sea, and Indian Ocean are warmer (cooler) than normal approximately 3–6 months after the peak warming (cooling) of SSTs in the central equatorial Pacific. We propose the following explanation: anomalies in atmospheric circulation associated with ENSO induce changes in the evaporation and cloud cover which, in turn, alter the net heat flux entering these remote oceans. These heat flux anomalies lead to the local SST anomalies that appear in conjunction with ENSO events. Although the relative magnitude and seasonality of cloud and latent heat flux anomalies varies between regions, the observational evidence presented in this paper supports this view. Taken as a whole, these relationships are consistent with the concept of an atmospheric bridge linking SST anomalies in the Pacific to SST anomalies in the remote tropical ocean basins (Lau 1997).

For the Indian Ocean, two caveats must be added. First, the changes in cloud cover associated with altered summer monsoons are observed to *lead* the ENSO index by approximately 3 months. Indeed, the fact that cloud cover leads the ENSO index by 3 months may explain why the lag time for the maximum SST correlation (Fig. 1) is shorter in the Indian Ocean (3 months) than in the South China Sea (5 months) or the tropical North Atlantic (6 months). The occurrence of anomalous cloud cover in the Indian Ocean sector prior to extreme swings in the ENSO index suggests a more complicated interaction between ENSO and the Asian monsoon that has not been addressed here. One possible explanation is that the Asian summer monsoon is linked to the distribution of springtime Pacific SST anomalies in years of developing El Niños or La Niñas (Ju and Slingo 1995). The second caveat is that we were unable to match SST anomalies in the southwestern portion of the Indian Ocean to any local anomalies in cloud cover or latent heat flux. It may be that changes in surface wind field over the Indian Ocean alter oceanic dynamics and cause some of the SST anomalies in this region. However, it should be borne in mind that cloud cover anomalies are prevalent over most of the Indian Ocean and that it is the northeastern Indian Ocean that has the strongest lagged correlation of SST to the ENSO index (Fig. 2c).

If the atmospheric bridge is responsible for the ENSO-related SST anomalies in the remote ocean basins, then predictions of the state of ENSO may be used to forecast the interannual variability at distant sites (Hastenrath 1995). Indeed, when the GFDL climate GCM is run with historical SSTs in the Pacific and with a mixed layer ocean outside of the Pacific (Lau and Nath 1996), it simulates teleconnections in tropical SSTs similar to those documented in this paper. We hope to report fully on these experiments in future articles.

APPENDIX

Ship Data Analysis

We use a compilation of individual ship reports in an extended version of the Edited Cloud Report Archive (ECRA; Hahn et al. 1996). As source material ECRA starts with the Compressed Marine Reports and Long Marine Reports archives of the Comprehensive Ocean Atmosphere Data Set (COADS; see Woodruff et al. 1987) and processes only those ship observations that have valid cloud information. The Extended ECRA (EECRA) differs from ECRA in that the ship-observed sea level pressure, wind speed and direction, surface air temperature, dewpoint depression, and sea surface temperature are passed unaltered from the COADS dataset to the EECRA dataset. Another difference between EECRA and ECRA is that the EECRA dataset has been processed for the years 1952–92, whereas the ECRA has been processed for the years 1982–91 only. In our study we only calculated total cloud cover from the observations which satisfied the illuminance criterion of Hahn et al. (1996). We have chosen to use the EECRA over the standard COADS data because of the higher level of quality control applied to the cloud information.

The individual ship observations were averaged to form monthly means on an irregularly spaced grid encompassing the region 30°N–30°S. The grid was designed to yield approximately the same number of ship observations per month for each box. The areas of these grid boxes over the tropical oceans are typically 5° lat × 10° long in the Atlantic and Indian Oceans but 5° lat

× 20° long in the Pacific. The density of the grid boxes can be seen from the wind vectors plotted on Figs. 7, 8, and 9.

An advantage of starting with the individual ship reports is that we can estimate the upward fluxes of sensible and latent heat for each individual report, and then average to form monthly means [as is done for the climatology compiled by da Silva and Levitus (1994)]. For each individual ship observation, the upward fluxes of sensible and latent heat were computed using the bulk formulas of Smith (1988). The Smith lookup tables give the exchange coefficients as functions of the 10-m air minus sea surface virtual potential temperature difference and the 10-m wind speed. Because ships commonly measure the wind speed at a typical mast height of 25 m whereas the air temperature and humidity are measured at a deck level near 10 m (J. Elms 1993, personal communication), the wind speed for each observation was multiplied by 0.93. The factor 0.93 is the similarity theory reduction of wind speed from the 25-m level to the 10-m level under neutral conditions (Isemer and Hasse 1991).

The assumption that the wind speed was measured at 25 m above the sea surface is clearly problematic since it is known that the average height of ship decks and masts has been increasing with time, thus resulting in an artificial interdecadal trend of increasing surface wind speeds (Cardone et al. 1990; Ward and Hoskins 1996), and of increasing sensible and latent heat fluxes. From the ship data we noted an increase in the tropical (30°N–30°S) mean latent heat flux from 105 W m^{-2} in the early 1950s to 135 W m^{-2} in the early 1990s (not shown). Since we are interested in ENSO variability and not interdecadal variability, the linear trend over the period 1952–92 was removed from each time series of sensible and latent heat flux. This procedure is effective in removing the artificial trend in reported wind speeds (Ward and Hoskins 1996).

REFERENCES

Angell, J. K., 1981: Comparison of variations in atmospheric quantities with SST variations in equatorial eastern Pacific. *Mon. Wea. Rev.,* **109,** 230–243.

Cardone, V. J., J. G. Greenwood, M. A. Cane, 1990: On trends in historical marine wind data. *J. Climate,* **3,** 113–127.

Charles, C. D., D. E. Hunter, and R. G. Fairbanks, 1997: Interaction between the ENSO and the Asian monsoon in a coral record of tropical climate. *Science,* **277,** 925–928.

Chiu, L. S., and R. E. Newell, 1983: Variations of zonal mean SST and large-scale air–sea interaction. *Quart. J. Roy. Meteor. Soc.,* **109,** 153–168.

daSilva, A. M., and S. Levitus, 1994: *Anomalies of Heat and Momentum Fluxes.* Vol. 3, *Atlas of Surface Marine Data,* U.S. Department of Commerce, 413 pp.

Deser, C., and J. M. Wallace, 1990: Large-scale atmospheric circulation features of warm and cold episodes in the tropical Pacific. *J. Climate,* **3,** 1254–1281.

——, and M. L. Blackmon, 1995: On the relationship between tropical and North Pacific sea surface temperature variations. *J. Climate,* **8,** 1677–1680.

Enfield, D. B., and D. A. Mayer, 1997: Tropical Atlantic sea surface temperature variability and its relation to El Niño–Southern Oscillation. *J. Geophys. Res.,* **102,** 929–945.

Frankignoul, C., 1985: Sea surface temperature anomalies, planetary waves and air–sea feedback in the middle latitudes. *Rev. Geophys.,* **23,** 357–390.

Fu, R., W. T. Liu, and R. E. Dickinson, 1996: Response of tropical clouds to the interannual variation of SST. *J. Climate,* **9,** 616–634.

Hahn, C. J., S. G. Warren, and J. London, 1996: Edited synoptic cloud reports from ships and land stations over the globe, 1982–1991. DOE Rep. NDP026B, 45 pp. [Available from Carbon Dioxide Information Analysis Center, Oak Ridge National Laboratory, P.O. Box 2008, Oak Ridge, TN 37831-6335.]

Harrison, E. F., P. Minnis, B. R. Barkstrom, V. Ramanathan, R. D. Cess, and G. G. Gibson, 1990: Seasonal variation of cloud radiative forcing derived from the Earth Radiation Budget Experiment. *J. Geophys. Res.,* **95,** 18 687–18 703.

Hastenrath, S., 1995: Recent advances in tropical climate prediction. *J. Climate,* **8,** 1519–1532.

——, L. C. de Castro, and P. Aceituno, 1987: The Southern Oscillation in the tropical Atlantic sector. *Beitr. Phys. Atmos.,* **60,** 447–463.

Inamdar, A. K., and V. Ramanathan, 1994: Physics of greenhouse effect and convection in warm oceans. *J. Climate,* **7,** 715–731.

Isemer, H., and L. Hasse, 1991: The scientific Beaufort equivalent scale: Effects on wind statistics and climatological air–sea flux estimates in the North Atlantic Ocean. *J. Climate,* **4,** 819–836.

Jones, P. D., and Coauthors, 1986: A global grid point surface air temperature data set: 1851–1984. NDP-020, 86 pp. [Available from Carbon Dioxide Information Analysis Center, Oak Ridge National Laboratory, P.O. Box 2008, Oak Ridge, TN 37831-6335.]

Ju, J., and J. M. Slingo, 1995: The Asian summer monsoon and ENSO. *Quart. J. Roy. Meteor. Soc.,* **121,** 1133–1168.

Julian, P. R., and R. M. Chervin, 1978: Study of the Southern Oscillation and Walker circulation phenomenon. *Mon. Wea. Rev.,* **106,** 1433–1451.

Kiladis, G. N., and H. F. Diaz, 1989: Global climatic anomalies associated with extremes in the Southern Oscillation. *J. Climate,* **2,** 1069–1090.

Lanzante, J. R., 1996: Lag relationships involving tropical SSTs. *J. Climate,* **9,** 2568–2578.

Lau, K.-M., and S. Yang, 1996a: The Asian monsoon and predictability of the tropical ocean–atmosphere system. *Quart. J. Roy. Meteor. Soc.,* **122,** 945–957.

——, and ——, 1996b: Seasonal variation, abrupt transition, and intraseasonal variability associated with the Asian summer monsoon in the GLA GCM. *J. Climate,* **9,** 965–985.

Lau, N.-C., 1997: Interactions between global SST anomalies and the midlatitude atmospheric circulation. *Bull. Amer. Meteor. Soc.,* **78,** 21–33.

——, and M. J. Nath, 1996: The role of the atmospheric bridge in linking tropical Pacific ENSO events to extratropical SST anomalies. *J. Climate,* **9,** 2036–2057.

Levitus, S., 1982: *Climatological Atlas of the World Ocean.* NOAA Prof. Paper 13, U.S. Government Printing Office, Washington, DC, 173 pp.

Meehl, G. A., 1987: The annual cycle and interannual variability in the tropical Pacific and Indian Ocean regions. *Mon. Wea. Rev.* **115,** 27–50.

Nobre, P., and J. Shukla, 1996: Variations of sea surface temperature, wind stress, and rainfall over the tropical Atlantic and South America. *J. Climate,* **9,** 2464–2479.

Oort, A. H., and J. J. Yienger, 1996: Observed long-term variability in the Hadley and Walker circulation and its connection to ENSO. *J. Climate,* **9,** 2751–2767.

Pan, Y. H., and A. H. Oort, 1983: Global climate variations connected with SST anomalies in the eastern equatorial Pacific ocean for 1958–1973 period. *Mon. Wea. Rev.,* **111,** 1244–1258.

Rasmusson, E. M., and T. H. Carpenter, 1983: The relationship be-

tween eastern equatorial Pacific SSTs and rainfall over India and Sri Lanka. *Mon. Wea. Rev.,* **111,** 517–528.

Reed, R. K., 1977: On estimating insolation over the ocean. *J. Phys. Oceanogr.,* **7,** 482–485.

Reynolds, R. W., and D. C. Marsico, 1993: An improved real-time global sea surface temperature analysis. *J. Climate,* **6,** 114–119.

Rossow, W. B., and R. A. Schiffer, 1991: International Satellite Cloud Climatology Project (ISCCP) cloud data products. *Bull. Amer. Meteor. Soc.,* **72,** 2–20.

Schmetz, J., and Coauthors, 1995: Monthly mean large-scale analyses of upper tropospheric humidity and wind field divergence derived from three geostationary satellites. *Bull. Amer. Meteor. Soc.,* **76,** 1578–1584.

Shaw, P.-T., S.-Y. Chao, K.-K. Liu, S.-C. Pai, and C.-T. Liu, 1996: Winter upwelling off Luzon in the northeastern south China Sea. *J. Geophys. Res.,* **101,** 16 435–16 448.

Smith, S. D., 1988: Coefficients for sea surface wind stress, heat flux, and wind profiles as a function of wind speed and temperature. *J. Geophys. Res.,* **93,** 15 467–15 472.

Smith, T. M., R. W. Reynolds, R. E. Livezey, and D. C. Stokes, 1996: Reconstruction of historical sea surface temperatures using empirical orthogonal functions. *J. Climate,* **9,** 1403–1420.

Soden, B. J., 1998: Tracking upper tropospheric water vapor radiances: A satellite perspective. *J. Geophys. Res.,* **103,** 17 069–17 081.

——, and F. P. Bretherton, 1996: Interpretation of TOVS water vapor radiances in terms of layer-average relative humidities: Method and climatology for the upper, middle and lower troposphere. *J. Geophys. Res.,* **101,** 9333–9343.

Tourre, Y. M., and W. B. White, 1995: ENSO signals in global upper-ocean temperature. *J. Phys. Oceanogr.,* **25,** 1317–1332.

Trenberth, K. E., and D. J. Shea, 1987: On the evolution of the Southern Oscillation. *Mon. Wea. Rev.,* **115,** 3078–3096.

Wallace, J. M., and D. S. Gutzler, 1981: Teleconnections in the geopotential height field during the Northern Hemisphere winter. *Mon. Wea. Rev.,* **109,** 784–812.

Ward, M. N., and B. J. Hoskins, 1996: Near-surface wind over the global ocean, 1949–1988. *J. Climate,* **9,** 1877–1895.

Webster, P. J., and S. Yang, 1992: Monsoon and ENSO: Selectively interactive systems. *Quart. J. Roy. Meteor. Soc.,* **118,** 877–926.

Woodruff, S. D., R. J. Slutz, R. L. Jenne, and P. M. Steurer, 1987: A Comprehensive Ocean–Atmosphere Data Set (COADS). *Bull. Amer. Meteor. Soc.,* **68,** 1239–1250.

Wu, M. C., and S. Hastenrath, 1986: On the interannual variability of the Indian monsoon and the Southern Oscillation. *Arch. Meteorol. Geophys. Bioclimatol.,* **36,** 239–261.

Yulaeva, E., and J. M. Wallace, 1994: The signature of ENSO in global temperature and precipitation fields derived from the microwave sounding unit. *J. Climate,* **7,** 1719–1736.